Annealing High Aspect Ratio Microgels into Macroporous 3D Scaffolds Allows for Higher Porosities and Effective Cell Migration

*Alisa C. Suturin, Andreas J. D. Krüger, Kathrin Neidig, Nina Klos, Nina Dolfen, Michelle Bund, Till Gronemann, Rebecca Sebers, Anna Manukanc, Ghazaleh Yazdani, Yonca Kittel, Dirk Rommel, Tamás Haraszti, Jens Köhler, and Laura De Laporte**

Growing millimeter-scaled functional tissue remains a major challenge in the field of tissue engineering. Therefore, microporous annealed particles (MAPs) are emerging as promising porous biomaterials that are formed by assembly of microgel building blocks. To further vary the pore size and increase overall MAP porosity of mechanically stable scaffolds, rod-shaped microgels with high aspect ratios up to 20 are chemically interlinked into highly porous scaffolds. Polyethylene glycol based microgels (width 10 µm, lengths up to 200 µm) are produced via in-mold polymerization and covalently interlinked into stable 3D scaffolds via epoxy-amine chemistry. For the first time, MAP porosities can be enhanced by increasing the microgel aspect ratio (mean pore sizes ranging from 39 to 82 µm, porosities from 65 to 90%). These porosities are significantly higher compared to constructs made from spherical or lower aspect ratio rod-shaped microgels. Rapid filling of the pores by either murine or primary human fibroblasts is ensured as cells migrate and grow extensively into these scaffolds. Overall, this study demonstrates that highly porous, stable macroporous hydrogels can be achieved with a very low partial volume of synthetic, high aspect ratio microgels, leading to large empty volumes available for cell ingrowth and cell–cell interactions.

1. Introduction

Hydrogels are widely investigated for promoting tissue regeneration by mimicking the extracellular matrix (ECM), which provides structural support to cells and plays an important role in controlling cell behavior.[1] Biochemical, mechanical, and physical cues can be introduced into the hydrogels to enhance cell spreading, proliferation, and invasion.[2] For cells to effectively replace the hydrogel matrix with their own ECM, the hydrogels are rendered hydrolytically or enzymatically degradable.

In vitro, cells are encapsulated inside the hydrogel to grow 3D cell cultures and tissue mimetics. Here, cells are mixed with the hydrogel precursors before crosslinking. Over time, these entrapped cells remodel their surrounding environment by spreading, proliferating, and migrating, while secreting ECM proteins into newly opened spaces as the gel degrades.[3] To promote the full transition from single encapsulated cells inside a hydrogel into fully functional tissue, efficient cell–cell interaction must be ensured. Furthermore, it is crucial to precisely tune the hydrogel degradation rate via molecular design and/or crosslinking density. Here, the optimal equilibrium between cell proliferation, ECM production, and hydrogel degradation must be found as a mismatch leads to the formation of fibrotic tissue, insufficient scaffolding, or even the collapse of the hydrogel network.[3a,4] Additionally, local changes in mechanical

---

A. C. Suturin, A. J. D. Krüger, K. Neidig, N. Klos, N. Dolfen, M. Bund, T. Gronemann, R. Sebers, A. Manukanc, G. Yazdani, Y. Kittel, D. Rommel, T. Haraszti, J. Köhler, L. De Laporte
DWI – Leibniz-Institute for Interactive Materials
Forckenbeckstraße 50, 52074 Aachen, Germany
E-mail: delaporte@dwi.rwth-aachen.de

The ORCID identification number(s) for the author(s) of this article can be found under https://doi.org/10.1002/adhm.202200989

DOI: 10.1002/adhm.202200989

A. C. Suturin, A. J. D. Krüger, Y. Kittel, D. Rommel, T. Haraszti, J. Köhler, L. De Laporte
Institute of Technical and Macromolecular Chemistry (ITMC)
Polymeric Biomaterials
RWTH University Aachen
Worringerweg 2, 52074 Aachen, Germany

L. De Laporte
Advanced Materials for Biomedicine (AMB)
Institute of Applied Medical Engineering (AME)
University Hospital RWTH Aachen
Center for Biohybrid Medical Systems (CMBS)
Forckenbeckstraße 55, 52074 Aachen, Germany

properties caused by cells remodeling the matrix can negatively impact local cell behavior.[5]

For in vivo applications, hydrogel precursor solutions can be injected in a minimally-invasive way and form a hydrogel locally to promote the formation of new healthy tissue with cells replacing the hydrogel material via native ECM production. Here, acellular bulk hydrogels can be employed as ECM mimetics with the goal to attract endogenous cells and thereby stimulate new tissue formation. In contrast to the previously described approach where cells remodel the hydrogel from the inside out, here endogenous cells migrate from the surrounding native tissues into the gel, which remains challenging as conventional synthetic hydrogels are nanoporous and thereby have to be degraded to enable cell infiltration.[5,6] In the case of enzymatic degradation on cell demand, cells infiltrate the hydrogels very slowly due to secretion/degradation kinetics and remaining steric hindrance.[4a,7] On the other hand, hydrogel degradation induced solely by hydrolysis is difficult to control and when too rapid leads to loss of structural support inside the gel before cells can reach the center of the gel.[8]

To overcome the limits of cell infiltration and cell–cell interaction, microporous injectable hydrogels have recently been developed.[8,9] Micropores were introduced during or after hydrogel formation using techniques such as porogen-leaching,[10] template removal,[11] phase separation,[12] or freeze drying.[13] However, most of these techniques are not cell compatible, which requires scaffold formation to be performed ex vivo without cells, followed by subsequent cell seeding in vitro or implantation inside the body. To form macroporous hydrogels in the presence of cells, pore formation after injection can be achieved using hydrogels with cell-friendly porogens,[14] nanocomposite hydrogels with a minimal amount of molecular crosslinkers,[15] or phase separation.[16]

Although the abovementioned methods have enabled cell movement inside open hydrogel constructs, they are still limited in pore interconnectivity, pore size, mechanical strength, and stability, depending on the technique. To overcome these challenges, a bottom-up assembly method was developed, in which spherical micron-sized hydrogel building blocks (microgels) are assembled into scaffolds with microscopic pores, called granular hydrogels.[17] If the microgels are covalently interlinked (annealed), the resulting scaffolds are called microporous annealed particles (MAPs).[4a] For example, microgels with a diameter of ≈150 µm resulted in MAPs with pore sections up to 45 µm (mean pore size 35 µm).[4a] Generally, for MAPs made from spherical microgels, porosities of up to 40% have been reached.[18] These injectable scaffolds offer more control over the mechanical properties (high porosities without losing mechanical integrity of the constructs) and biochemical signals (facile introduction of biological cues).

So far, MAPs are mostly made from spherical microgels produced via microfluidics. Rapid microgel or particle annealing is realized by for example click reactions (e.g., thiol-ene Michael addition[4a,18,19]), guest–host interactions,[20] or physical crosslinking of two oppositely charged building blocks.[3a,21] The result is a microporous network with interstitial spaces between the microgels available for cell ingrowth and ECM deposition.[19a,22] Such MAPs were able to accelerate cutaneous tissue regeneration and tissue structure formation in opened wounds (100 versus 40% wound closure for employed MAPs versus non-porous hydrogels, 5 days after injection).[4a] However, perfectly spherical microgels can form close-packed lattices, minimizing interstitial space with the pore sizes depending on the microgels' diameter. Since a more interconnected open network with larger pores improves the depth and rate of cell penetration,[] a strong need remains for developing scaffolds with improved pore characteristics including interconnectivity, size, and total porosity.[24]

Two recent studies suggested that scaffolds built from rod-shaped microgels show improved pore features.[25] In the first study, scaffolds made from either spherical or rod-shaped microgels were compared in porosity, and pore interconnectivity (in silico, in vitro, and in vivo). Here, microgels were produced via thiol-ene photo-crosslinking using norbornene-modified hyaluronic acid and dithiothreitol, and further assembled into 3D macroporous constructs without covalently interlinking the microgels together. Both spherical and rod-shaped microgels had a cross-sectional diameter of 100 µm, with the rod-shaped microgels having a relatively low aspect ratio of 2.2. Scaffolds made from both shapes had comparable overall porosity (15 to 25% depending on the jamming method) and pore sizes (10^3 to 10^4 µm^2 depending on the jamming method) but the assemblies made from rod-shaped microgels demonstrated a more interconnected pore network with anisotropic tubular-like pore shapes. Thereby, in vitro endothelial sprouting after 3 days of cell culture and in vivo endogenous cell migration 1 week after injection were enhanced in the scaffolds prepared from rod-shaped microgels.[25b]

In the second study, reported by our group, MAPs were formed by assembling and covalently interlinking rod-shaped, polyethylene glycol (PEG)-based microgels. Here, microgels with complementary reactive groups were chemically connected via epoxy-amine addition and acted as viable scaffolds for cell infiltration and growth, as well as ECM secretion. The anisometric microgels had a length of up to 640 µm and aspect ratios varying from 2.2 to 4.5, resulting in pore sizes ranging from 25 to 225 µm and mean pore sizes around 100 µm. These pore sizes were ≈4.5-fold larger compared to similar scaffolds made from spherical microgels.[25a] In this system, rapid crosslinking fixated the rod-shaped microgels in their jammed state, not giving them time to form densely packed stacks. This explains the larger pore sizes compared to scaffolds made from microgels that are not covalently interlinked, and thus may build a more nematic ordered scaffold. Over 7 days, fibroblasts covered all microgel surfaces and after 23 days, filled up the pores of the scaffold.

We hypothesize that by significantly increasing the aspect ratio of the microgels, the pore sizes and overall porosity of the respective MAPs can be increased. To test this and overcome limitations of currently employed spherical and low aspect ratio (< 5), rod-based microgels for bottom-up assemblies, we present for the first time the assembly and interlinking of high aspect ratio (5–20), rod-shaped microgels into macroporous scaffolds. Anisometric microgel building blocks are produced via in-mold polymerization as already published previously by our group.[26] The microgels have a width of 10 µm and a varying length from 50 to 200 µm, and are rigid and hard to deform due to their high stiffnesses. Amine functionalities are incorporated into the microgel network to allow for subsequent interlinking (varied from 17 to 29 wt%). Via amine-epoxy reaction, the microgels are annealed into macroporous networks using an epoxy-functionalized six-armed PEG molecule as interlinking agent. The resulting scaffolds show high porosities up to 90% with mean pore sizes up to 84 µm. With increasing microgel aspect ratio from 5 to 20, the porosities increase from 65 to 90%, and the mean pore sizes of the scaffolds from 39 to 82 µm, supporting our hypothesis. After functionalizing the microgel surface with cell adhesive short peptides (GRGDSPC), fibroblasts migrate into these macroporous networks, proliferate, and rapidly fill the interconnected pore network after a culture of 7 days, which is significantly faster compared to the ≈23 days required for the larger rod-shaped microgels with smaller aspect ratio.[25a]

2. Results and Discussion

2.1. Rod-Shaped Microgels Assembled into Macroporous Scaffolds

The rod-shaped microgels used in the two previous MAP studies are produced via microfluidics—a high-yield process.[25] However, reliable microgel downscaling in size is challenging as the microgel diameter is depending on the channel size. Furthermore, a high batch to batch variation is often observed due to variations in flow rates, temperature, and other environmental conditions. In this study, microgels are fabricated via an in-mold fabrication technique called particle replication in nonwetting templates (PRINT).[26] PRINT allows for the precise, independent control of microgel shape, size, and composition with low batch to batch variation as the crosslinking takes place under static conditions in the controlled environment of a nitrogen chamber.[8] As a drawback, PRINT is a batch process that results in lower microgel yields compared to microfluidics. To circumvent these issues, a continuous roll-to-roll production of PRINTed particles has been published by the DeSimone lab.[27]

In this study, anisometric, monodisperse microgels are fabricated via copolymerizing PEG diacrylate (PEG-DA, 700 g mol^{-1}) and 2-aminoethyl methacrylate (AEMA) via PRINT. Three different microgel compositions with varying amounts of AEMA (17, 24, and 29 wt%) are photo-crosslinked in-mold under inert gas atmosphere for 1 h. The exact microgel compositions can be found in Table S1, Supporting Information. In this work, microgels of three different aspect ratios are fabricated by varying their length; $10 \times 10 \times 50$ µm^3 (aspect ratio 5), $10 \times 10 \times 100$ µm^3 (aspect ratio 10), and $10 \times 10 \times 200$ µm^3 (aspect ratio 20). The produced microgels precisely recapture the shape of the cavities of the PDMS masters, as shown in **Figure 1**A.

Microgel stiffness is investigated using nanoindentation (Figure 1B). Here, the effective Young's moduli decrease from ≈470 ± 37 kPa for microgels containing 17 wt% AEMA to 65 ± 8 kPa for microgels containing 29 wt% AEMA. This trend could be explained by an increasing ratio of monofunctional AEMA to bifunctional PEG-DA, resulting in less crosslinked microgel networks.[28] Furthermore, the free amine groups of the AEMA building blocks are reported to have a pK_a of 7.6.[29] Hence, their positive charge at neutral pH can cause an increased water uptake.[30] To test this, the degree of microgel swelling is investigated at neutral pH in deionized water (Figure 1C,D). With increasing AEMA concentration, microgels show an enhanced swelling behavior supporting our explanation.

For inter-microgel annealing, free amine groups on the microgel surface are interlinked with an epoxy-functionalized, six-armed star-shaped poly(ethylene oxide-*stat*-propylene oxide) (sPEG-epoxy). sPEG-epoxy is synthesized as described previously by our group with 20% statistically distributed propylene oxide and a molecular weight of ≈18 000 g mol^{-1} (number average).[31] The interlinking agent is diluted to an aqueous solution (60 wt%) and the desired amount of rods is added dropwise. Amine-epoxy interlinking takes place immediately without the requirement of catalysts or elevated temperatures.[32] If not mentioned differently, the total unswollen microgel volume is kept constant (0.945 mm^3) throughout all scaffolds presented in this study by interlinking 200 000 ($10 \times 10 \times 50$ µm^3), 100 000 ($10 \times 10 \times 100$ µm^3), or 50 000 ($10 \times 10 \times 200$ µm^3) microgels into one assembly. Scaffolds made from this microgel volume have macroscopic dimensions of ≈5 mm in length, 4 mm in width, and 1 mm in thickness (measured after washing and when floating in deionized water). To allow for optimal scaffold formation, the mixture containing rods and sPEG-epoxy is centrifuged for faster settlement. The microgels do not stack but are randomly arranged as can be seen in Movie S1, Supporting Information. Generally, the size of the MAP scaffolds can be easily upscaled—in **Figure 2**A, for example, 400 000 microgels (1 microgel: $10 \times 10 \times 100$ µm^3, total microgel volume: 3.78 mm^3) are annealed into a larger scaffold with a volume of ≈400 mm^3. If sPEG-epoxy is diluted to concentrations below 60 wt%, 3D microgel assemblies start to fragment into smaller pieces (Figure S1, Supporting Information). Macroscopic and microscopic images of the scaffolds can be found in Figure 2A–C. As shown in Movie S2, Supporting Information, the scaffolds withstand strong mechanical stress without fracturing as they do not get damaged by compressing the scaffold with a tweezer. To further investigate the mechanical integrity and the influence of microgel AEMA content, rheological testing is performed. In Figure 2D, the storage modulus of the 3D assemblies is shown for the different microgel compositions. Even though there is a deviation caused by the larger, irregular pores, a clear trend of increasing storage modulus for MAPs made from microgels with higher AEMA content can be observed. In more detail, the storage moduli increase from 30 ± 23 kPa (17 wt% AEMA) to 185 ± 110 kPa (29% AEMA). Interestingly, this trend is opposed to the decreasing individual microgel stiffness with increasing AEMA content (effective Young's modulus 65 kPa for 29 wt% AEMA versus 470 kPa for 17 wt% AEMA, Figure 1B). Hence, the increase of available interlinking groups, resulting in more mechanically stable MAP networks, seems to have a more significant impact than the single microgel stiffnesses.

Minimum void distances between neighboring microgels are automatically determined by analyzing individual images of the z-stacks and estimating a skeleton between the microgels determining the maximum distance from all "walls." Afterward, the obtained output data are binned and visualized in a histogram using an R script. Exemplary images of this process can be found in Figure S2, Supporting Information. Throughout this study, the mean of these distances is referred to as mean pore size. As shown in **Figure 3**, MAP porosity can be controlled by varying the microgel aspect ratio (while changing the AEMA content of the microgel does not affect porosities, Figure S3, Supporting Information). Scaffolds made from microgels with dimensions

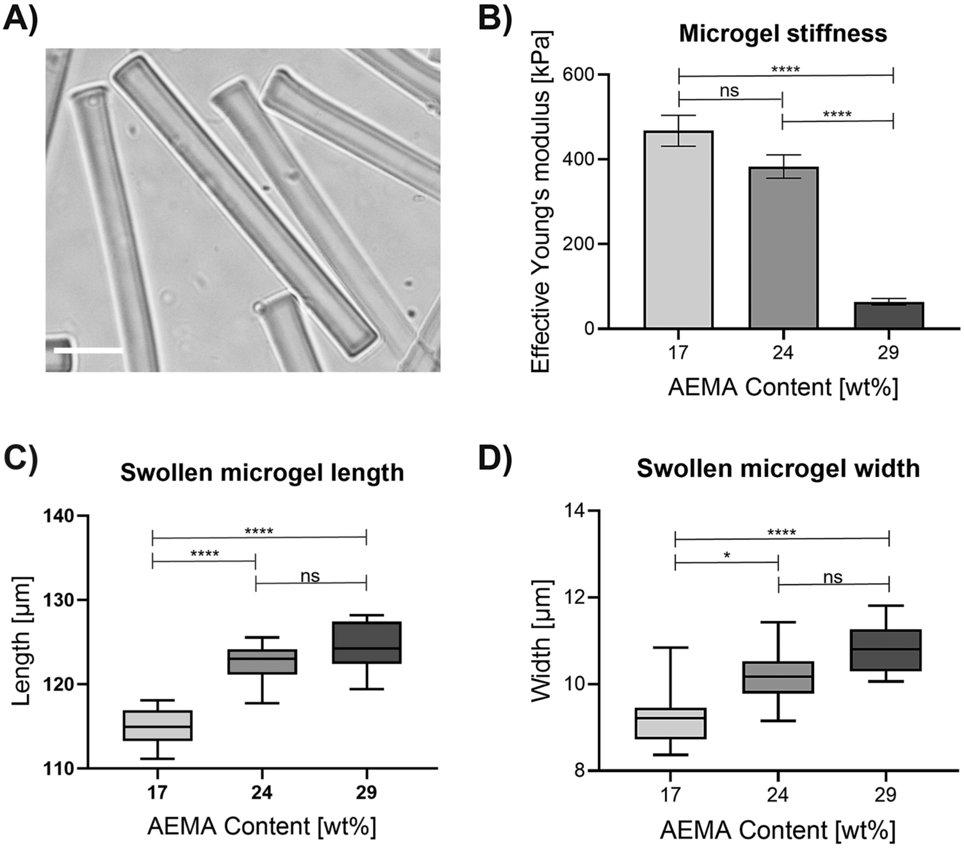

Figure 1. Microgel properties influenced by AEMA concentration. A) Brightfield microscopy image showing rod-shaped microgels (29 wt% AEMA, dimensions: 10 × 10 × 100 µm^3). Scale bar 20 µm. B) Effective Young's modulus determined via nanoindentation showing the influence of different AEMA concentrations. Three separately prepared microgel batches are measured ($n = 3$; per microgel batch, three microgels are averaged). Error bars represent ± SEM, and p-values are determined using one-way ANOVA with post-hoc Tuckey's test, ****$p < 0.0001$, ns non-significant. C) Swollen microgel length (unswollen length after in-mold polymerization: 100 µm) and D) microgel width (unswollen width after in-mold polymerization: 10 µm) in deionized water depending on AEMA concentration. The lengths and widths of three separately prepared microgel batches are measured ($n = 3$; per microgel batch, three microgels are averaged) and are determined using ImageJ. The line inside the box represents the median. The whiskers present minimum and maximum values, and p-values are determined using one-way ANOVA with post-hoc Tuckey's test, non-significant (ns) $p \geq 0.05$, *$p < 0.015$, ****$p < 0.0001$.

10 × 10 × 50 µm^3 show a mean pore size of 39 ± 7 µm (mean ± SEM), while with an increasing aspect ratio of the microgel building blocks, larger mean pore sizes are obtained. Scaffolds made from microgels with the dimensions of 10 × 10 × 100 µm^3 show a mean pore size of 50 ± 2 µm, and scaffolds made from 10 × 10 × 200 µm^3 microgels have a mean pore size of 82 ± 2 µm. The pore size distribution of the scaffolds made from the microgels of 10 × 10 × 200 µm^3 is more polydisperse, and positively skewed. Overall porosities are compared by analyzing the interstitial void space between microgels of respective confocal z-projections. Here, the porosity enhances from ≈65%, 75%, to 90% for increasing aspect ratios of 5 to 10 to 20, respectively.

Previously, porosity of MAPs made from spherical microgels was controlled by increasing the volume of the utilized building blocks.[33] For example, Griffin et al. reported an increase in mean pore size from 10 to 35 µm by changing the microgel diameters from 30 µm ($V \approx 520$ µm^3) to 150 µm ($V \approx 22\,500$ µm^3). Hence, the mean pore size was increased by 3.5-folds by increasing the microgel volume by ≈45 times.[4a] By changing the shape of the MAP building blocks from spherical to rod-shaped, our group achieved significantly increased mean pore sizes of ≈100 µm compared to MAPs made from comparable spherical microgels (porosities ≈60%). No significant change in porosity was observed by increasing the microgel aspect ratio from 2.2 to 4.5.[25a] The present study shows that the microgel aspect ratio indeed influences MAP porosity. The here reported porosities match previously stated porosities of MAPs made from microgels with comparable aspect ratio (here: 65% for aspect ratio 5, previous report ≈60% for aspect ratio 4.5[25a]). By increasing the microgel aspect ratio from 5 to 20, a 1.4-fold increase in porosity is observed resulting in notably high porosities of up to 90%.

Commonly, significantly softer microgels are annealed into MAPs.[4a,7,18,19b] The microgels used in this study are more rigid, and harder to bend or deform. Besides annealing rod-shaped microgels of higher aspect ratios, this fact likely also contributed to obtaining those high porosities.

Furthermore, we used building blocks of high microgel volume (V up to 8 000 000 µm^3) in our previous study.[25a] In this study, the microgels have a significantly decreased microgel volume ($V \approx 5000$ to 20 000 µm^3) that is up to 400-fold lower com-

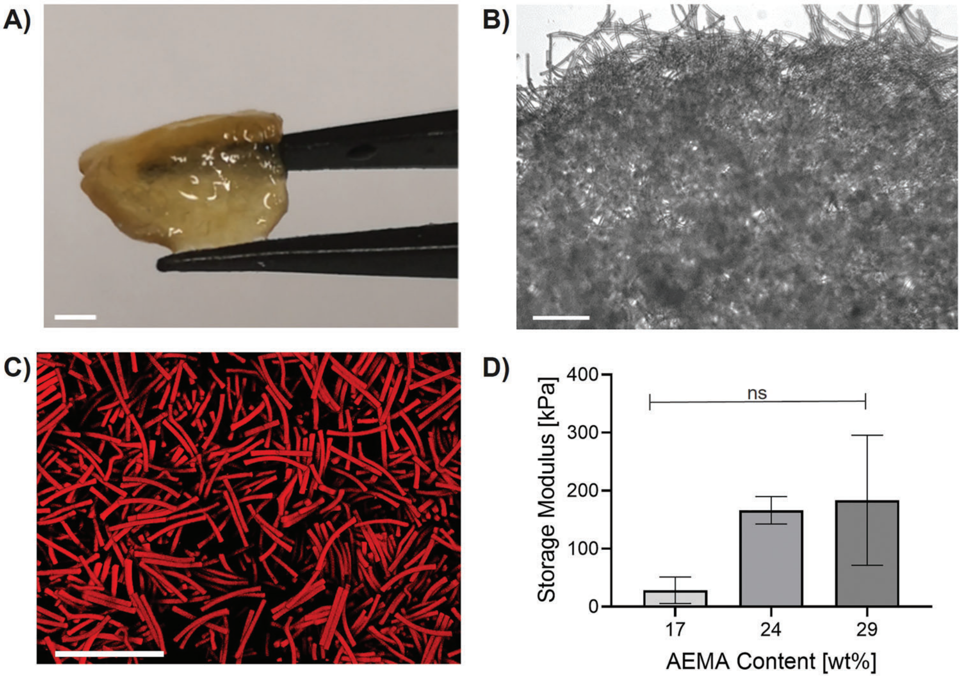

Figure 2. Assembly characterization. Assemblies made from 400 000 rod-shaped microgels (29 wt% AMEA, dimensions: 10 × 10 × 100 µm^3) to produce large constructs, recorded with A) Leica dual camera showing the full macroscopic scaffold (scale bar 4 mm), B) brightfield microscopy showing the border of the scaffold (scale bar 100 µm), and C) confocal microscopy showing random microgel fixation inside the scaffold (scale bar 100 µm). D) Storage moduli obtained via rheological measurements. The mean out of at least three different scaffolds is shown (error bars represent ± SEM). *P*-values are determined using one-way ANOVA with post-hoc Dunnett's test, non-significant (ns) $p \geq 0.05$, $^*p < 0.05$.

pared to the previously reported rod-shaped microgels. Importantly, the reduced volume of microgels did not significantly decrease the obtained mean pore sizes due to the enhanced aspect ratio from 2.2–4.5 (mean pore size 100 µm) to 20 (mean pore size 82 µm). Therefore, large pore sizes can be obtained with a much smaller fraction of total microgel volume compared to previously annealed anisotropic MAP building blocks. Hence, the porosities are remarkably higher, varying from 65% up to 90% for aspect ratios increasing from 5 to 20, respectively. To the best of our knowledge, these are the highest porosities reported so far for MAPs. Thereby, we demonstrate that in order to obtain larger pores, it is more beneficial to increase the aspect ratios of rod-shaped MAP building instead of increasing the microgel volume.

For in vivo application of MAPs, two strategies can be followed, to inject microgels and form the MAPs in vivo or to produce them ex vivo and sequentially implant or inject them as a 3D construct. As the scaffolds can withstand enormous mechanical stress (Movie S2, Supporting Information), they can be transferred very easily using a tweezer, spatula, or a pipette (5 mL pipette for scaffolds made from a total microgel volume of 0.945 mm^3, see Figure S4, Supporting Information). To enable injection of pre-formed MAPs via shear-thinning or self-healing properties or for in vivo scaffold formation, the MAPs in this report would require an alternative interlinking chemistry. In addition, one can imagine automated pipetting systems to form the presented MAPs and grow ex vivo tissue models, for example for drug testing. Furthermore, we believe that specific shapes can be obtained in the future by 3D bioprinting or in-mold scaffold formation.

2.2. Cell Growth into 3D MAP Scaffolds

To evaluate the applicability of these macroporous scaffolds for tissue regeneration, mouse-derived L929 cells are seeded on the scaffolds and cell infiltration and growth are investigated. Therefore, 5000 cells are seeded onto the sterilized scaffolds and cultured for 7 days. In order to ensure cell adhesion, the microgels are functionalized with a cell-adhesive peptide GRGDSPC before scaffold formation (immunohistological staining of GRGDS, Figure S5, Supporting Information). Furthermore, the cell inserts are pre-coated with Sigmacote to reduce surface adsorption of the cells and improve cell–scaffold interaction (Figure S6, Supporting Information). Here, the thiol group of the end-standing cysteine is covalently bound to remaining unreacted acrylates of PEG-DA inside the microgel network via thiol-Michael click reaction. 750 000 microgels are suspended overnight in a phosphate buffered solution ($pH = 8.5$) containing $36{\bullet}10^{-3}$ M of the peptide.

In a first step, the influence of the AEMA concentration on cell behavior is investigated for microgels with the dimensions 10 × 10 × 100 µm^3 (**Figure 4**). The AEMA content in the microgels does not have a significant influence on the mean pore size of the scaffolds as shown in Figure S3, Supporting Information. After allowing the cells to grow and migrate into the constructs for 7 days, the remaining void spaces (not occupied by cells, or microgels) are compared by analyzing the z-projections of superimposed confocal z-stacks. All scaffolds made from microgels containing the three different AEMA concentrations are filled by L929 cells that migrated into the porous construct and proliferated to fill the pores without significant differences in

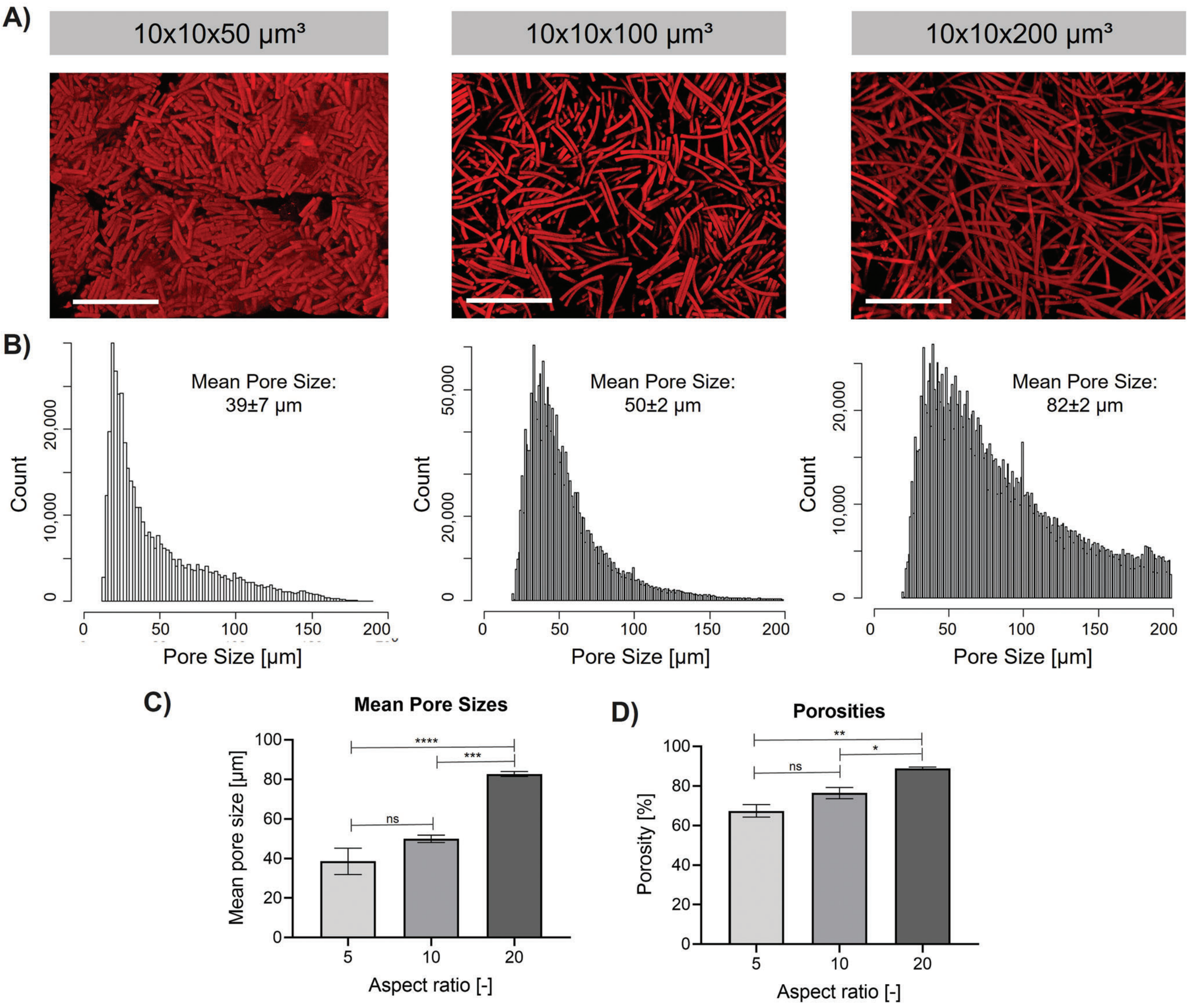

Figure 3. Microgel aspect ratio influencing the porosity of 3D microgel scaffolds. MAPs are made from microgels containing 29% AEMA with varying aspect ratios from 5 to 20. A) Projection images after superposition of z-stack images of microgel scaffolds recorded in confocal microscopy of MAPs made from microgels of different aspect ratios. Scale bar 200 µm. B) Pore size distribution determined based on single images obtained in the respective z-stack. Confocal Z-stacks are analyzed by applying a python script to determine pore sizes, and output data are binned and visualized using an R-script. C) Comparison of mean pore sizes obtained by the respective python script. D) Comparison of porosities obtained by the respective python script using the projection images of the respective z-stacks. The mean out of at least three different scaffolds is shown (error bars represent ± SEM). *P*-values are determined using one-way ANOVA with post-hoc Tuckey's test, non-significant (ns) $p \geq 0.05$, $^{*}p < 0.05$, $^{**}p < 0.005$, $^{***}p < 0.0005$, $^{****}p < 0.0001$.

remaining void spaces and metabolic activities (MTS assay on days 1 and 7 Figure 4C). This suggests that there is no influence of varying AEMA content on cell proliferation. Regions in which the scaffold is not optimally interlinked result in remaining void spaces as the pores were too large to be filled in the 7-days culturing time (unfilled volume percentage up to 27% for scaffolds made from microgels containing 17 wt% AEMA). In previously published MAPs made from significantly larger building blocks, cells initially predominantly grow on the 2D surfaces of the building blocks and sequentially fill the interstitial spaces after covering the microgel surfaces.[25a] As the MAP building blocks used in this study are significantly smaller, the cells growing inside of these scaffolds attach to and bridge multiple neighboring microgels at a time, as can be seen in the enlarged images of Figure 4. Interestingly, Figure S6, Supporting Information shows distinct differences in cell morphology depending on the AEMA content of the respective microgels. For scaffolds made with 17 wt% AEMA, cells adhere and grow well but their morphology is rather round. By increasing the AEMA concentration, the cells spread more, suggesting an improved cell–microgel interaction. These results are consistent with observations previously made by our group suggesting that an increased AEMA concentration supports cell adhesion and spreading, likely due to the increased positive charges at physiological conditions.[25a]

Next, cell growth on and into scaffolds made from microgels of different ratios is investigated as presented in **Figure 5**.

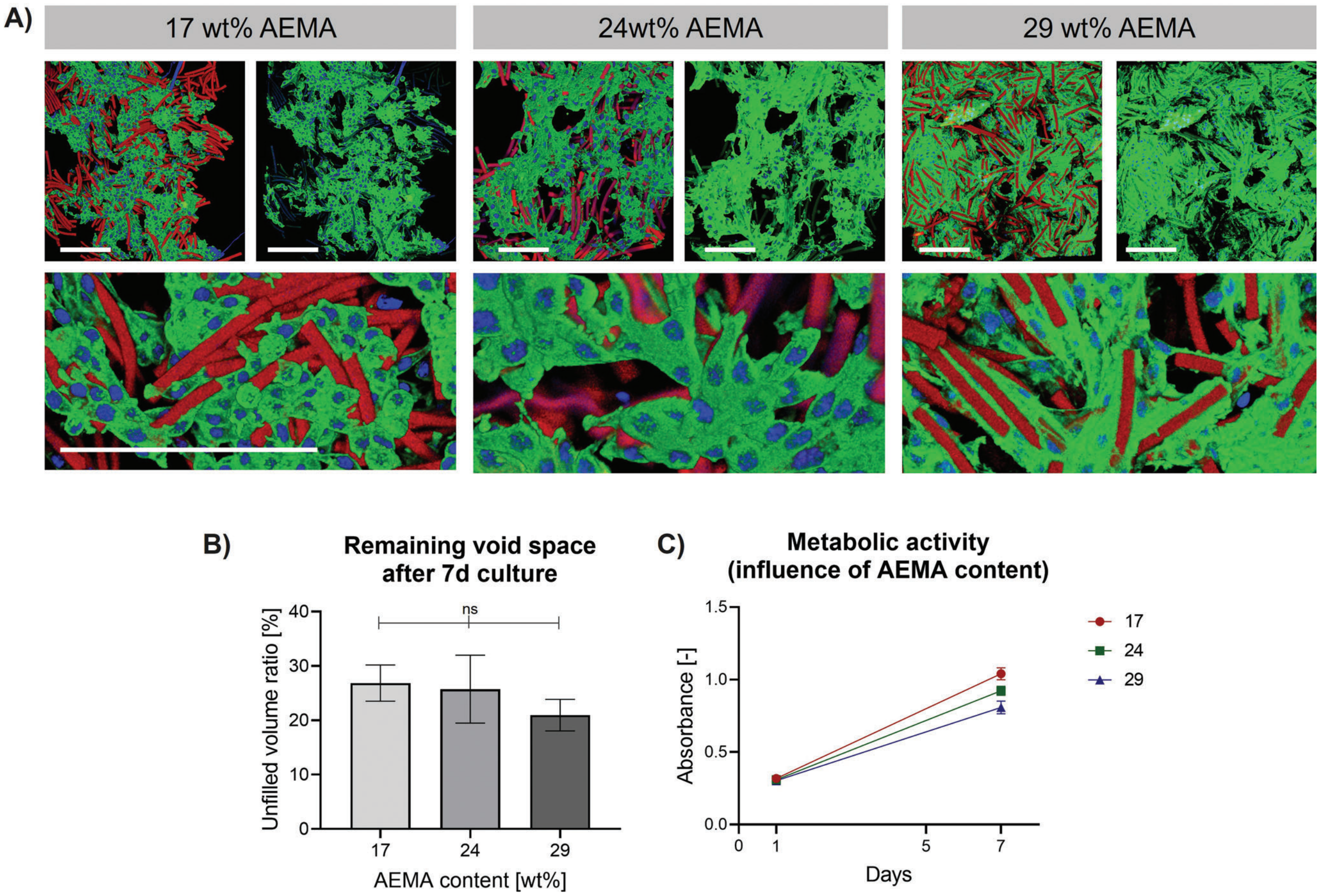

Figure 4. Influence of AEMA concentration in microgel rods on L929 cell spreading after 7d cell culture. A) Z-projection images after superposition of z-stack confocal images of MAPs made from rod-shaped microgels (10 × 10 × 100 µm^3) containing different AEMA concentrations. Microgels are shown in red, F-actin in green, and cell nuclei in blue. Scale bar 200 µm. B) Percentage of unfilled volume (not occupied by microgels or cells) remaining in the assemblies after 7 days of culture determined by analyzing respective confocal z-stack projections with a python script. The mean out of at least 3 different scaffolds is shown (error bars represent ± SEM). *P*-values are determined using one-way ANOVA, non-significant (ns) $p \geq 0.05$. C) Metabolic activities influenced by AEMA content after 1 and 7 days of culturing L929 cells. The activity is determined with MTS assay (Promega, CellTiter 96 AQueous One Solution Cell Proliferation Assay). The mean out of 3 different scaffolds is shown (error bars represent ± SEM). A two-way repeated measures analysis of variance (ANOVA) shows an effect of time ($F(1, 6) = 867.4$, $^{****}p < 0.0001$), an effect of AEMA content ($F(2,6) = 6.001$, $^{*}p < 0.05$) and an interaction of both values ($F(2,9) = 9.001$, $^{*}p < 0.05$).

Here, all scaffolds are prepared using microgels containing 29 wt% AEMA. As mentioned above, acellular scaffolds made from microgels with this AEMA content showed mean pore sizes and porosities of ≈39 µm and 65% (scaffolds made from 10 × 10 × 50 µm^3 microgels), ≈50 µm and 75% (scaffolds made from 10 × 10 × 100 µm^3 microgels), and ≈82 µm and 90% (scaffolds made from 10 × 10 × 200 µm^3 microgels). After 7 days of cell culture, the following trend is observed: the remaining void space decreases by culturing MAPs made from microgels of lower aspect ratio. Scaffolds made from 10 × 10 × 50 µm^3, 10 × 10 × 100 µm^3, or 10 × 10 × 200 µm^3 sized microgels, show remaining void spaces of ≈10%, 20%, and 30%. As already described above, cells predominantly grow in the interstitial space attaching and spreading to and onto various microgels at once. Only regions bearing larger pores are not completely filled with cells, leading to the respective remaining void space ratios. As the MAPs made from higher aspect ratio microgels bear a higher number of larger pores (Figure 3B), the previously described trend can be explained. Interestingly, in the case of scaffolds made from 10 × 10 × 200 µm^3 sized microgels, cells predominantly attach to one microgel and cover its surface instead of immediately bridging the pores between the microgels. After 14 days of cell culture, the cells filled up the larger pores and less free volume is available in all conditions. The scaffolds made from 10 × 10 × 50 µm^3, 10 × 10 × 100 µm^3, or 10 × 10 × 200 µm^3 sized microgels, show remaining void spaces of ≈10%, 6%, and 4%, respectively (Figure 3D). As shown in Figure 3E, the metabolic activities are increasing with time suggesting continuous proliferation in all conditions. When comparing the remaining void spaces, it is important to keep in mind that the total volume is larger for the high aspect ratio microgels. Interestingly, the cells do not further fill the remaining empty space inside the MAPs made of 10 × 10 × 50 µm^3 microgels, while the void spaces of the MAPs made from higher aspect ratio microgels keep decreasing after day 7. The remaining open space (≈10%) is likely because, as shown in Figure 3B,

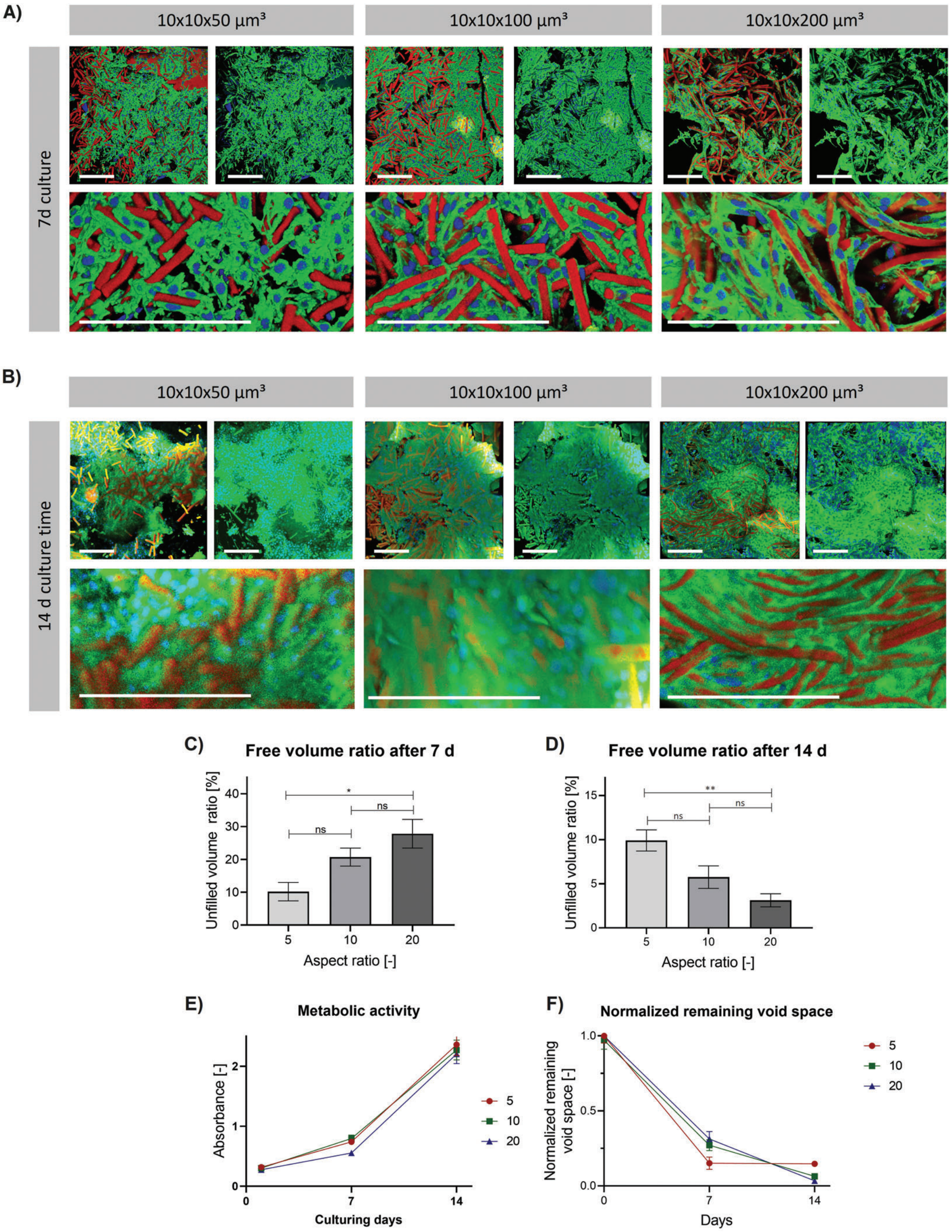

Figure 5. L929 cell growth into microgel assemblies made from microgels of different aspect ratios after 7 or 14 day cell culture. Z-projection images after superposition of z-stack confocal images of MAPs made from microgels of varying aspect ratios (5 to 20) with constant AEMA content (29 wt%) after A) 7 days or B) 14 days of cell culture. Confocal z-stack images show the cell growth into assemblies. Microgels are shown in red, F-actin in green, and cell nuclei in blue. Scale bar 200 µm. Percentage of unfilled volume (not occupied by microgels or cells) remaining in the assemblies after C) 7 days or D) 14 days of culture determined by analyzing respective confocal z-stack projections with a python script. The mean out of at least 3 different scaffolds is shown (error bars represent ± SEM). *P*-values are determined using one-way ANOVA with post-hoc Tuckey's test, non-significant (ns) $p \geq 0.05$, $^{*}p < 0.05$, $^{**}p < 0.01$. E) Metabolic activities influenced by microgel aspect ratio after 1, 7, and 14 days of culturing L929 cells. The activity is determined with MTS assay (Promega, CellTiter 96 AQueous One Solution Cell Proliferation Assay). The mean out of at least 3 different scaffolds is shown (error bars represent ± SEM). A two-way repeated measures analysis of variance (ANOVA) shows an effect of time ($F(1.167, 7.004) = 325.5$, $^{****}p < 0.0001$), non-significant effect of microgel aspect ratio ($F(2, 6) = 1.364$, $p = 0.3248$) and non-significant interaction of both values ($F(4, 12) = 0.3963$, $p = 0.8076$). F) Change of normalized remaining void space over time. The mean out of 3 different scaffolds is shown (error bars represent ± SEM). Each time point is normalized by dividing the determined void space (shown in (C,D)) by the starting void space at day 0. A two-way repeated measures analysis of variance (ANOVA) shows an effect of time ($F(1.433, 7.167) = 483.4$, $^{****}p < 0.0001$), a non-significant effect of microgel aspect ratio ($F(2, 6) = 0.1639$, $p = 0.8525$) and an interaction of both variables ($F(4, 10) = 3.738$, $^{*}p < 0.05$).

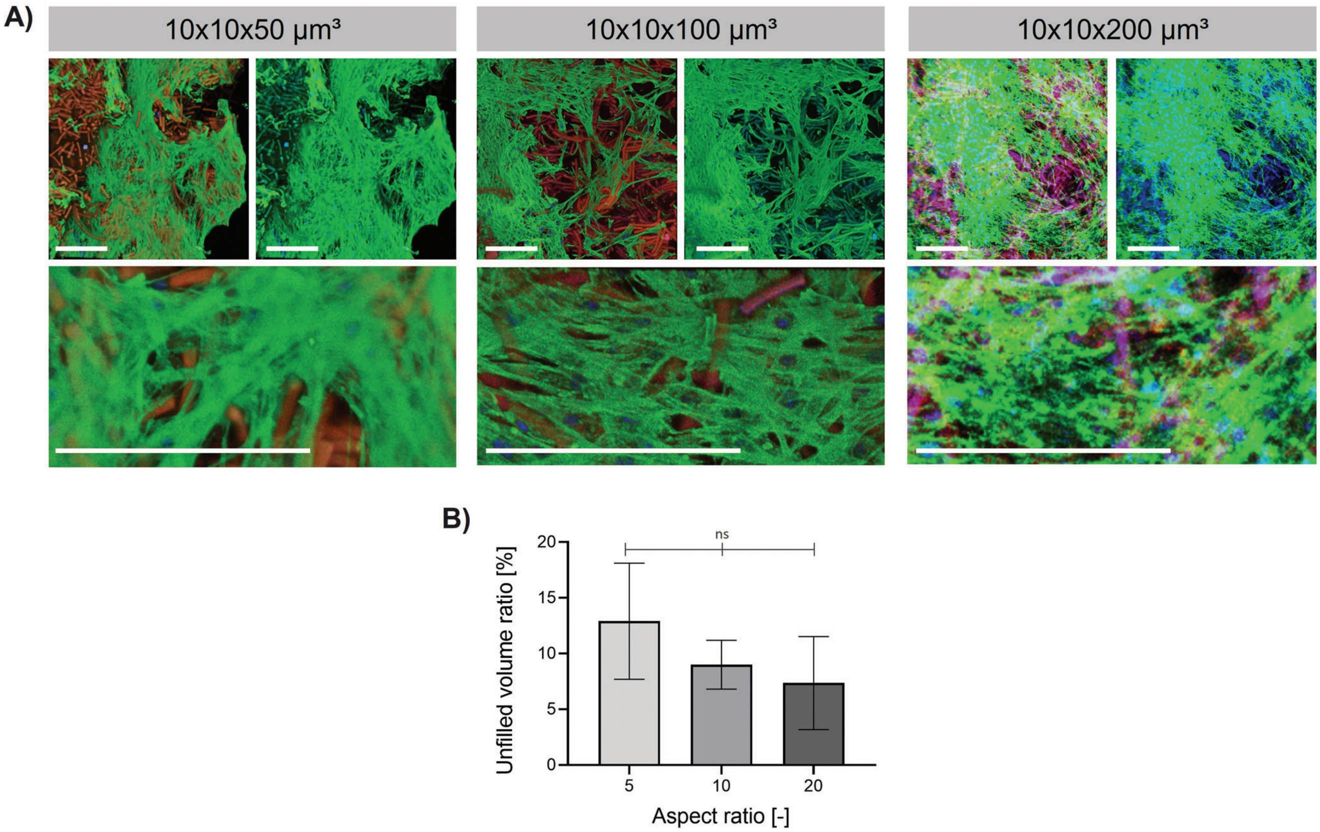

Figure 6. Influence of microgel aspect ratio on NHDF cell spreading after 7d of cell culture. A) Z-projection images after superposition of z-stack confocal images of MAPs made from rod-shaped microgels (containing 29 wt% AEMA) with changing aspect ratios. Microgels are shown in red, F-actin in green, and cell nuclei in blue. Scale bar 200 μm. B) Percentage of unfilled volume (not occupied by microgels or NHDF cells) remaining in the assemblies after 7 days of culture determined by analyzing respective confocal z-stack projections with a python script. The mean out of at least 3 different scaffolds is shown (error bars represent ± SEM). *P*-values are determined using one-way ANOVA, non-significant (ns) $p \geq 0.05$.

scaffolds made from higher aspect ratio microgels have less smaller pores. The remaining unfilled pores in the scaffold made from the $10 \times 10 \times 50$ μm^3 microgels seem to be either completely filled with ECM proteins or too small to be filled by L929 cells and thus, they remain unfilled with cells. The scaffolds made from higher aspect ratio microgels, however, contain less smaller pores, which results in the cells being able to fill the scaffold more efficiently. This hypothesis is supported when the change in free volume inside the entire MAP is plotted over time and normalized by the starting free volume at day 0, thus the ratio of free volume at a specific time in culture and the initial free volume before cells are added (Figure 3F). Here, the normalized void space of the MAPs made of $10 \times 10 \times 50$ μm^3 microgels stagnates at 15% after day 7. While the void spaces of both MAPs made from higher aspect ratio microgels keep decreasing, the filling rate of the MAPs made from $10 \times 10 \times 100$ μm^3 microgels slows down compared to the MAPs made from $10 \times 10 \times 200$ μm^3 microgels. This supports our hypothesis that the MAPs made from the higher aspect ratio microgels have fewer pores that are too small to be penetrated by cells. As 23 days of cell culture were needed to fill the pores in the previously reported anisotropic MAP system,[25a] the cell infiltration rate observed in the scaffolds of this study is more rapid.

To show transferability from the murine L929 cell line to human more clinically relevant cell types, primary normal human dermal fibroblasts (NHDFs) are seeded onto the scaffolds as done earlier with L929 cells and cultured for 7 days. The cells are spreading intensively over the whole construct. No significant difference in the remaining void space can be observed when comparing MAPs made from the three different aspect ratio microgels, but following trend can be identified: scaffolds made from $10 \times 10 \times 50$ μm^3, $10 \times 10 \times 100$ μm^3, or $10 \times 10 \times 200$ μm^3 sized microgels show remaining void spaces of ≈12% (L929s after 7 d 10%, after 14 d 10%), 9% (L929s after 7 d 20%, after 14 d 6%), and 4% (L929s after 7 d 30%, after 14 d 3%). As shown in **Figure 6**C, primary NHDFs fill the pores faster than murine L929s. This observation is in line with previously published results.[25a] In our case, culturing NHDFs for 7 d in scaffold made from the highest aspect ratio microgels resulted in the same remaining void spaces of scaffolds cultured with L929s for 14 d.

Furthermore, it is possible to form scaffolds by diluting sPEG-epoxy in cell media instead of water. Stable constructs are obtained, however showing a decreased mean pore size of 38 ± 2 μm and overall porosity of ≈31% compared to annealing in water (Figure S7, Supporting Information). As the supplemented cell media contains free amines and thiols available for deactivating the epoxy interlinking agent, fewer interlinking functionalities are available resulting in a slower scaffold formation. Hence, microgels annealed in water are fixated in the jammed state, while annealing in cell medium might allow for a more nematic order of the rods resulting in decreased porosities. This explanation is supported by analyzing the anisotropy of the scaffolds using the ImageJ plugin FibrilTool.[34] This plugin was developed to analyze fibrillar structures giving among other things an anisotropy score (value between 0 and 1, while 0 depicts isotropy and 1 anisotropy). Here, scaffolds annealed in water are indeed more isotropic (anisotropy score 0.011 ± 0.003) compared to scaffolds annealed in media (anisotropy factor 0.023 ± 0.001). As presented in Figure S8, Supporting Information, cells cultured for 7 days on these scaffolds also show extensive cell growth and fill all average-sized pores with only 8% of the remaining uncovered volume. For future applications of the system, this might be very interesting to encapsule cells during scaffold formation as for example relevant for 3D bioprinting. However, the annealing procedure must be optimized to avoid too high centrifugation speeds or, for example, potentially cytotoxically high sPEG-Epoxy concentrations.

As the rate and depth of cell penetration depend on pore size and interconnectivity,[35] we believe that MAPs made from rod-shaped microgels of high aspect ratio and low microgel volume can induce effective and rapid cell infiltration at a higher rate compared to the larger rod-shaped microgels. Interestingly, the highest aspect ratio of 20 leads to higher cell/microgel interaction and alignment of the cells along the long axis of the microgel. This seems to slow down the pore filling ability of the cells as they then have less of a microgel bridging function. For the successful transformation from hydrogel-based artificial ECM to new native, healthy tissue, the synthetic material must be degraded and replaced by cells and their native ECM.[36] Therefore, systems with higher porosities (less synthetic material) are desired. On the other hand, upon microgel degradation, the scaffold needs to maintain its stability, thus the degradation rate and cell growth need to be in tune with each other. The degradation of thinner, higher aspect ratio microgels will create smaller voids compared to larger microgels, thus avoiding local loss of mechanical scaffold integrity, and leading to more reliable formation of new tissue.

3. Conclusion

In this study, we present the assembly of high-aspect-ratio microgels into stable, interlinked 3D scaffolds. Compared to previously reported scaffolds made from softer, low-aspect-ratio microgels of larger volume, the scaffolds in this study show increased porosities from 65 up to 90% and mean pore sizes from 39 to 82 µm for microgel aspect ratios varying from 5 to 20, respectively. Hence, we show that MAP porosity can indeed be controlled by varying microgel aspect ratios in contrast to previously published results. The obtained individual pore sizes of the MAP scaffolds after microgel annealing are comparable to previously published systems while the total microgel volume is drastically decreased. We believe that this system offers very promising properties for facile cell infiltration and improved cell–cell interaction. On the one hand, the extensive pore network ensures rapid and deep cell invasion, while on the other hand, the significantly smaller microgels will leave smaller voids when degraded, thus maintaining scaffold stability while promoting tissue formation. Furthermore, the highly porous architecture of the scaffolds presented in this study can be further altered and biological/physical cues can be easily introduced. Thereby, we believe that the here presented MAPs made from high-aspect-ratio microgels present a promising bottom-up material system for future application in tissue regeneration.

4. Experimental Section

Rod-Shaped Microgels Assembled into Macroporous Scaffolds: The microgel production was adapted from previously reported methods.[26c,e] In the following, the steps are described shortly.

The PDMS molds (Sylgard 184 polymer kit, Dow Corning) were produced as negative replicates to fluorosilanized silicon wafers, containing rectangular features of 10 × 10 × 50 µm^3, 10 × 10 × 100 µm^3, or 10 × 10 × 200 µm^3.

For microgel fabrication, 500 µL PEG-DA (700 g mol^{-1}, Sigma Aldrich) was mixed with 35.9 µL of a 10 wt/v% 2-hydroxy-4′-(2-hydroxy-ethoxy)-2-methylpropiophenone (Irgacure 2959, BASF) solution and 24.1 µL ethanol (70 v%). Depending on the desired microgel composition (see Table S1, Supporting Information), the respective mass of AEMA (m_{AEMA}: 93.6 mg, 133.5 mg, or 162.0 mg) was dissolved in 414 µL PEG-filler (200 g mol^{-1}). For preparing the final crosslinking solution, 30 µL of phosphate buffer (pH = 8.5) and 111, 111, or 105 µL of the PEG-DA/irgacure stock solution ($V_{\mathrm{PEG\text{-}DA/IRG}}$) was added to the AEMA stock solution. The resulting solution contains 17, 24, or 29 wt% AEMA. After mixing thoroughly, the solution was cast on the PDMS mold and pressed into its channels. By using a sacrificial polyethylene terephthalate (PET) sheet (Goodfellow GmbH), the excess crosslinking solution was removed from the PDMS mold surface while the cavities remain filled. Crosslinking was performed for 60 min under UV exposure in a constant nitrogen atmosphere. The mold filled with the cured microgels was fixed on a glass slide using a 50 wt% polyvinylpyrrolidone (PVP, Sigma Aldrich) and dried for 5 d at room temperature. To harvest the microgels, the mold was peeled off and the microgels were suspended in deionized water. The microgels were purified by centrifuging at 4500 rpm for 10 min followed by replacing the supernatant until PVP residues have been removed. The microgel concentration was determined using a Neubauer chamber and set to 6000 rods µL^{-1} (rod dimension: 10 × 10 × 50 µm^3), 3000 rods µL^{-1} (rod dimension: 10 × 10 × 100 µm^3), or 1500 rods µL^{-1} (rod dimension: 10 × 10 × 200 µm^3) to keep the total volume of microgels (before swelling) constant at 0.945 mm^3.

Pre-Assembly Surface Functionalization with GRGDSPC: For pre-assembly RGD functionalization, the microgel suspension (250 µL, 7.5 mm^3 total microgel volume) was centrifuged for 10 min at 4500 rpm and the supernatant was discarded. The remaining microgel pellet was resuspended in 250 µL phosphate buffer (pH = 8.5) and 5 µL of aqueous GRGDSPC solution (25 mg mL^{-1}) was added. The suspension was stored overnight at 4 °C to allow the thiol on the cysteine to react with the remaining free acrylates. After RGD coupling, the suspension was centrifuged again, after which the supernatant was discarded and replaced with deionized water. This washing step was repeated twice.

Microgel Assembly: 31.5 µL of the RGD-coupled microgel suspension were added dropwise to 100 µL on a 60 wt% sPEG-epoxy solution. sPEG-epoxy (18 kDa, 6-armed) was synthesized as described previously with all batches indicating a functionalization over 95%.[26e] The microgels in sPEG-epoxy were centrifuged for 10 min at 4500 rpm. After microgel interlinking overnight, the microgel assembly was transferred carefully into a sigmacoted cell culture insert for 24 well-plates equipped with a translucent membrane (Greiner Bio-one, pore size: 8 µm) and washed extensively with deionized water. For sigmacoting, the cell culture inserts were surface functionalized by soaking in Sigmacote (Sigma Aldrich) for a couple of seconds and drying overnight at room temperature.

Evaluating Microgel Stiffness via Nanoindentation: Microgel stiffness was investigated using the high-throughput mechanical screening platform Pavone (Optics11Life, Amsterdam, TheNetherlands). To ensure sufficient microgel attachment to the surface, 10 µL microgel suspension was added into an empty well of a 24 well plate and the water was allowed to evaporate overnight. On the next day, MilliQ was added to the well without detaching the microgels from the surface and the indentation measurements were performed in MilliQ at room temperature. Here, a cantilever-based probe with a spherical tip radius of 3.5 µm and a cantilever stiffness of 0.25 N m^{-1} was used (piezo speed 15 µm s^{-1}, indentation depth was 2 µm). Applying the Hertzian contact model,[37] the effective Young´s modulus E (kPa) was obtained from the respective indentation curves. For all microgel conditions, three separately prepared microgel batches were measured ($n = 3$). Per microgel batch, three microgels were averaged.

Evaluating Macroscopic Properties of MAP Scaffolds via Rheology: Rheological characterizations were performed on pre-interlinked, washed MAP scaffolds floating in MilliQ water using a DHR 3 Rheometer from TA instruments at 25 °C. A parallel plate geometry at 250 µm truncation gap was used. The time sweep measurements were recorded at 0.5 Hz frequency and 2% strain for 10 min. The storage modulus was determined by averaging all measured values.

Evaluating Pore Size Distribution of MAP Scaffolds: Individual images of confocal z-stacks were analyzed automatically using a python script. To remove the influence of neighboring slices, each image was blurred using a Gaussian kernel (standard deviation of 50 pixels, the window of the kernel was 301 pixels wide). The resulting images were subtracted as background, while negative pixel values were set to zero. Then the resulting images were smoothened with a second, narrower Gaussian kernel (standard deviation of 2 pixels, the window was 13 pixels wide). Pixels belonging to the microgels were identified by applying a threshold using Otsu's method. All pixels darker than this threshold were considered to be unfilled void space. Because the pore structure could not be separated into individual pore islands, a distance transform was applied, and the local maxima were searched in the resulting distance landscape, identifying lines of "ridges." The value of these pixels was the locally maximal value of the distance from the nearest edge of the pores. These values were collected for each image and turned into a statistical ensemble of pore sizes. Because the local maximum detector works using a gradient of the quadratic distance values with a typical minimum gradient value of 20 pixels, distances below 10 pixels were not registered. The distances were then scaled with the image resolution to micrometers. For each z-stack, the parameters of the Gaussian filters, the threshold calculation (Otsu's method or fixed relative threshold), and the minimum gradient size for the local maximum detector can be set by the user.

Evaluating Void Space Fraction/Porosity: In order to obtain an impression of the relative filled space of the scaffolds, the z-projection of superimposed confocal stacks was analyzed using a python script. The channels showing microgels, and F-actin of the cells were treated differently. The channel showing the microgels was background corrected using a blurred version of the image (negative values after subtracting the background were set to 0). This blurred version was created by convolving the image with a Gaussian kernel (standard deviation: 200 pixels, window of the filter 1201 pixels). The image of the channel showing the actin of the cells was not background corrected. Both channels were then smoothed with a Gaussian kernel (width: 1 pixel, window size 7 pixels).

The background was separated from the images cutting the intensity values at 10% of the maximum intensity in the image. Values above or below this threshold were set to 1 or 0 respectively. The ratio of object pixels to the whole area of the image was defined as covered, while the rest was the remaining unfilled void space (in the case of acellular MAPs porosity).

To normalize this void space (as done in Figure 6F), the remaining void spaces obtained as described above were divided by the starting void space without cells. All these data at various time points present unpaired data as scaffolds had to be fixed and it was not possible to image the exact same spot of the scaffold in confocal microscopy.

Cell Experiments: Mouse-derived L929 fibroblasts were cultured in DMEM media supplemented with 10 v% fetal bovine serum (FBS, Biowest) and 1 v% antibiotics/antimycotics (Gibco) at 37 °C and 5 v% CO_2. Before seeding the cells on the microgel assemblies, the sigmacoted cell culture inserts containing the microgel scaffolds were placed into ethanol (70 v%) and sterilized under UV-light in a sterile laminar flow environment for 40 min. After sterilization, the ethanol was removed. The assemblies were washed extensively with PBS, and subsequently with supplemented DMEM media. 5000 cells in 100 µL were added dropwise on top of the microgel assemblies. The inserts were then placed into respective wells filled with 500 µL supplemented DMEM media and incubated at 37 °C and 5 v% CO_2.

Immunocytochemical Staining and Confocal Microscopy: Samples were fixed with 4% paraformaldehyde (PFA, AppliChem) for 30 min, followed by washing the assemblies with PBS. Cell membrane permeabilization was induced by Triton X-100 (0.1 v% for 7 min). Then, the cells were stained with phalloidin-iFluor-488 (1/1000 in PBS) for 1 h and DAPI (1/100 in PBS) for 20 min.

Statistical Analysis: Data points are shown as mean average with error bars indicating the standard error of the mean (± SEM) with $n \geq 3$. Statistical analysis was performed using GraphPad Prism 8. Significance was determined by one-way analysis of variance (ANOVA) with post-hoc Tukey's test, two-way analysis of variance (ANOVA), or Welch's t-test. The p-values for statistical significance are represented with stars ($^*p < 0.05$, $^{**}p < 0.005$, $^{***}p < 0.0005$, $^{****}p < 0.0001$).

Supporting Information

Supporting Information is available from the Wiley Online Library or from the author.

Acknowledgements

The authors gratefully acknowledge funding from the Leibniz Senate Competition Committee (SAW) under the Professorinnenprogramm (SAW-2017-PB62: BioMat). The authors acknowledge funding from the Deutsche Forschungsgemeinschaft (DFG) within the project B5 and C3 SFB 985 "Functional Microgels and Microgel Systems." Furthermore, the authors sincerely acknowledge financial support from the European Commission (EUSMI, 731019). Parts of the analytical investigations were performed at the Center for Chemical Polymer Technology CPT, which was supported by the European Commission (EUSMI, no. 731019) and the Federal State of North Rhine-Westphalia (No. 300088302). The authors would like to gratefully thank Dr. Jacopo Di Russo for his inspiring discussions at Institute for Molecular and Cellular Anatomy (RWTH Aachen University), and Stefan Hauk at DWI for performing SEM measurements.

Open Access funding enabled and organized by Projekt DEAL.

Conflict of Interest

The authors declare no conflict of interest.

Data Availability Statement

The data that support the findings of this study are available from the corresponding author upon reasonable request.

Keywords

macroporous scaffolds, bottom-up assembly, high aspect ratio microgels, in-mold polymerization, 3D cell culture, tissue engineering

Received: April 29, 2022
Revised: August 25, 2022

[1] a) N. Chen, Z. Zhang, B. Soontornworajit, J. Zhou, Y. Wang, *Biomaterials* **2012**, *33*, 1353; b) H. Geckil, F. Xu, X. Zhang, S. Moon, U. Demirci, *Nanomedicine* **2010**, *5*, 469.

[2] a) B. Trappmann, B. M. Baker, W. J. Polacheck, C. K. Choi, J. A. Burdick, C. S. Chen, *Nat. Commun.* **2017**, *8*, 371; b) C. M. Madl, L. M. Katz, S. C. Heilshorn, *ACS Macro Lett.* **2018**, *7*, 1302.

[3] a) R.-S. Hsu, P.-Y. Chen, J.-H. Fang, Y.-Y. Chen, C.-W. Chang, Y.-J. Lu, S.-H. Hu, *Adv. Sci.* **2019**, *6*, 1900520; b) D. Seliktar, *Science* **2012**, *336*, 1124; c) A. J. Engler, S. Sen, H. L. Sweeney, D. E. Discher, *Cell* **2006**, *126*, 677; d) J. Zhu, R. E. Marchant, *Expert Rev. Med. Devices* **2011**, *8*, 607; e) C. M. Madl, S. C. Heilshorn, *Annu. Rev. Biomed. Eng.* **2018**, *20*, 21.

[4] a) D. R. Griffin, W. M. Weaver, P. O. Scumpia, D. Di Carlo, T. Segura, *Nat. Mater.* **2015**, *14*, 737; b) M. Guvendiren, J. A. Burdick, *Nat. Commun.* **2012**, *3*, 792; c) S. P. Zustiak, J. B. Leach, *Biomacromolecules* **2010**, *11*, 1348.

[5] H. Wang, S. C. Heilshorn, *Adv. Mater.* **2015**, *27*, 3717.

[6] a) J. J. Rice, M. M. Martino, L. De Laporte, F. Tortelli, P. S. Briquez, J. A. Hubbell, *Adv. Healthcare Mater.* **2013**, *2*, 57; b) H. Rogan, F. Ilagan, X. Tong, C. R. Chu, F. Yang, *Biomaterials* **2020**, *228*, 119579; c) O. Chaudhuri, J. Cooper-White, P. A. Janmey, D. J. Mooney, V. B. Shenoy, *Nature* **2020**, *584*, 535; d) S. Rhee, *Exp. Mol. Med.* **2009**, *41*, 858.

[7] J. Koh, D. R. Griffin, M. M. Archang, A.-C. Feng, T. Horn, M. Margolis, D. Zalazar, T. Segura, P. O. Scumpia, D. Di Carlo, *Small* **2019**, *15*, 1903147.

[8] S. Babu, F. Albertino, A. Omidinia Anarkoli, L. De Laporte, *Adv. Healthcare Mater.* **2021**, *10*, 2002221.

[9] a) Y.-C. Chiu, M.-H. Cheng, H. Engel, S.-W. Kao, J. C. Larson, S. Gupta, E. M. Brey, *Biomaterials* **2011**, *32*, 6045; b) *Tissue Eng., Part C* **2015**, *21*, 773; c) S. M. LaNasa, I. T. Hoffecker, S. J. Bryant, *J. Biomed. Mater. Res., Part B* **2011**, *96B*, 294; d) J. C. Rose, L. De Laporte, *Adv. Healthcare Mater.* **2018**, *7*, 1701067; e) K. J. De France, F. Xu, T. Hoare, *Adv. Healthcare Mater.* **2018**, *7*, 1700927.

[10] a) *Tissue Eng., Part C* **2010**, *16*, 905; b) Y. Gong, Q. Zhou, C. Gao, J. Shen, *Acta Biomater.* **2007**, *3*, 531.

[11] D. Lu, Z. Zeng, Z. Geng, C. Guo, D. Pei, J. Zhang, S. Yu, *Biomed. Mater.* **2022**, *17*, 025006.

[12] Y. Li, C. Zhu, D. Fan, R. Fu, P. Ma, Z. Duan, X. Li, H. Lei, L. Chi, *Int. J. Polym. Mater. Polym. Biomater.* **2020**, *69*, 505.

[13] M. H. Rich, M. K. Lee, N. Marshall, N. Clay, J. Chen, Z. Mahmassani, M. Boppart, H. Kong, *Biomacromolecules* **2015**, *16*, 2255.

[14] a) L. Griveau, M. Lafont, H. le Goff, C. Drouglazet, B. Robbiani, A. Berthier, D. Sigaudo-Roussel, N. Latif, C. L. Visage, V. Gache, R. Debret, P. Weiss, J. Sohier, *Acta Biomater.* **2022**, *140*, 324; b) L. Wang, S. Dong, Y. Liu, Y. Ma, J. Zhang, Z. Yang, W. Jiang, Y. Yuan, *Polymers* **2020**, *12*, 1138.

[15] F. Fiorini, E. A. Prasetyanto, F. Taraballi, L. Pandolfi, F. Monroy, I. López-Montero, E. Tasciotti, L. De Cola, *Small* **2016**, *12*, 4881.

[16] S. Taheri, G. Bao, Z. He, S. Mohammadi, H. Ravanbakhsh, L. Lessard, J. Li, L. Mongeau, *Adv. Sci.* **2022**, *9*, 2102627.

[17] M. Shin, K. H. Song, J. C. Burrell, D. K. Cullen, J. A. Burdick, *Adv. Sci.* **2019**, *6*, 1901229.

[18] S. Xin, O. M. Wyman, D. L. Alge, *Adv. Healthcare Mater.* **2018**, *7*, 1800160.

[19] a) C. M. Dumont, M. A. Carlson, M. K. Munsell, A. J. Ciciriello, K. Strnadova, J. Park, B. J. Cummings, A. J. Anderson, L. D. Shea, *Acta Biomater.* **2019**, *86*, 312; b) N. J. Darling, W. Xi, E. Sideris, A. R. Anderson, C. Pong, S. T. Carmichael, T. Segura, *Adv. Healthcare Mater.* **2020**, *9*, 1901391.

[20] a) A. E. Widener, M. Bhatta, T. E. Angelini, E. A. Phelps, *Biomater. Sci.* **2021**, *9*, 2480; b) J. E. Mealy, J. J. Chung, H.-H. Jeong, D. Issadore, D. Lee, P. Atluri, J. A. Burdick, *Adv. Mater.* **2018**, *30*, 1705912.

[21] Q. Feng, D. Li, Q. Li, X. Cao, H. Dong, *Bioact. Mater.* **2022**, *9*, 105.

[22] a) J. A. Finbloom, B. Demaree, A. R. Abate, T. A. Desai, *Adv. Funct. Mater.* **2020**, *30*, 2005938; b) F. Li, V. X. Truong, P. Fisch, C. Levinson, V. Glattauer, M. Zenobi-Wong, H. Thissen, J. S. Forsythe, J. E. Frith, *Acta Biomater.* **2018**, *77*, 48; c) Z. Hu, C. Ma, X. Rong, S. Zou, X. Liu, *ACS Appl. Mater. Interfaces* **2018**, *10*, 2377; d) L. Pruett, R. Ellis, M. McDermott, C. Roosa, D. Griffin, *J. Mater. Chem. B* **2021**, *9*, 7132.

[23] F. Bai, Z. Wang, J. Lu, J. Liu, G. Chen, R. Lv, J. Wang, K. Lin, J. Zhang, X. Huang, *Tissue Eng., Part A* **2010**, *16*, 3791.

[24] a) I. Bružauskaitė, D. Bironaitė, E. Bagdonas, E. Bernotienė, *Cytotechnology* **2016**, *68*, 355; b) N. Kazem, C. Majidi, C. E. Maloney, *Soft Matter* **2015**, *11*, 7877; c) B. Kessel, M. Lee, A. Bonato, Y. Tinguely, E. Tosoratti, M. Zenobi-Wong, *Adv. Sci.* **2020**, *7*, 2001419.

[25] a) D. Rommel, M. Mork, S. Vedaraman, C. Bastard, L. P. B. Guerzoni, Y. Kittel, R. Vinokur, N. Born, T. Haraszti, L. De Laporte, *Adv. Sci.* **2022**, *9*, 2103554; b) T. H. Qazi, J. Wu, V. G. Muir, S. Weintraub, S. E. Gullbrand, D. Lee, D. Issadore, J. A. Burdick, *Adv. Mater.* **2022**, *34*, 2109194.

[26] a) J. C. Rose, D. B. Gehlen, T. Haraszti, J. Kohler, C. J. Licht, L. De Laporte, *Biomaterials* **2018**, *163*, 128; b) J. C. Rose, M. Fölster, L. Kivilip, J. L. Gerardo-Nava, E. E. Jaekel, D. B. Gehlen, W. Rohlfs, L. De Laporte, *Polym. Chem.* **2020**, *11*, 496; c) J. C. Rose, M. Cámara-Torres, K. Rahimi, J. Köhler, M. Möller, L. De Laporte, *Nano Lett.* **2017**, *17*, 3782; d) A. Omidinia-Anarkoli, S. Boesveld, U. Tuvshindorj, J. C. Rose, T. Haraszti, L. De Laporte, *Small* **2017**, *13*, 1702207; e) A. J. D. Krüger, J. Köhler, S. Cichosz, J. C. Rose, D. B. Gehlen, T. Haraszti, M. Möller, L. De Laporte, *Chem. Commun.* **2018**, *54*, 6943.

[27] J. Xu, D. H. C. Wong, J. D. Byrne, K. Chen, C. Bowerman, J. M. DeSimone, *Angew. Chem., Int. Ed.* **2013**, *52*, 6580.

[28] a) P. T. Smith, B. Narupai, J. H. Tsui, S. C. Millik, R. T. Shafranek, D.-H. Kim, A. Nelson, *Biomacromolecules* **2020**, *21*, 484; b) M. B. Browning, T. Wilems, M. Hahn, E. Cosgriff-Hernandez, *J. Biomed. Mater. Res., Part A* **2011**, *98A*, 268.

[29] K. L. Thompson, E. S. Read, S. P. Armes, *Polym. Degrad. Stab.* **2008**, *93*, 1460.

[30] K. Chen, J. Xu, J. C. Luft, S. Tian, J. S. Raval, J. M. DeSimone, *J. Am. Chem. Soc.* **2014**, *136*, 9947.

[31] A. J. D. Kruger, J. Kohler, S. Cichosz, J. C. Rose, D. B. Gehlen, T. Haraszti, M. Moller, L. De Laporte, *Chem. Commun.* **2018**, *54*, 6943.

[32] J. M. Laza, C. A. Julian, E. Larrauri, M. Rodriguez, L. M. Leon, *Polymer* **1999**, *40*, 35.

[33] a) A. S. Caldwell, G. T. Campbell, K. M. T. Shekiro, K. S. Anseth, *Adv. Healthcare Mater.* **2017**, *6*, 1700254; b) C. M. Murphy, F. J. O'Brien, *Cell Adhes. Migr.* **2010**, *4*, 377.

[34] A. Boudaoud, A. Burian, D. Borowska-Wykręt, M. Uyttewaal, R. Wrzalik, D. Kwiatkowska, O. Hamant, *Nat. Protoc.* **2014**, *9*, 457.

[35] a) S. M. Lien, L. Y. Ko, T. J. Huang, *Acta Biomater.* **2009**, *5*, 670; b) N. Annabi, J. W. Nichol, X. Zhong, C. Ji, S. Koshy, A. Khademhosseini, F. Dehghani, *Tissue Eng., Part B* **2010**, *16*, 371.

[36] Y. Zhu, H. Jiang, S.-H. Ye, T. Yoshizumi, W. R. Wagner, *Biomaterials* **2015**, *53*, 484.

[37] H. Hertz, *J. für die Reine und Angew. Math.* **1882**, *1882*, 156.